Stereochemistry of the chloroperoxidase active site: crystallographic and molecular-modeling studies

M Sundaramoorthy[1], James Terner[2] and Thomas L Poulos[1]

Background: Chloroperoxidase (CPO) is the most versatile of the known heme enzymes. It catalyzes chlorination of activated C–H bonds, as well as peroxidase, catalase and cytochrome P450 reactions, including enantioselective epoxidation. CPO contains a proximal heme–thiolate ligand, like P450, and polar distal pocket, like peroxidase. The substrate-binding site is formed by an opening above the heme that enables organic substrates to approach the activated oxoferryl oxygen atom. CPO, unlike other peroxidases, utilizes a glutamate acid–base catalyst, rather than a histidine residue.

Results: The crystal structures of CPO complexed with exogenous ligands, carbon monoxide, nitric oxide, cyanide and thiocyanate, have been determined. The distal pocket discriminates ligands on the basis of size and pK_a. The refined CPO–ligand structures indicate a rigid active-site architecture with an immobile glutamate acid–base catalyst. Molecular modeling and dynamics simulations of CPO with the substrate *cis*-β-methylstyrene and the corresponding epoxide products provide a structural and energetic basis for understanding the enantioselectivity of CPO-catalyzed epoxidation reactions.

Conclusions: The various CPO–ligand structures provide the basis for a detailed stereochemical mechanism of the formation of the intermediate compound I, in which Glu183 acts as an acid–base catalyst. The observed rigidity in the active site also explains the relative instability of CPO compound I and the formation of the HOCl chlorinating species. Energetics of CPO–substrate/product molecular modeling provides a theoretical basis for the P450-type enantioselective epoxidation activities of CPO.

Addresses: [1]Department of Molecular Biology and Biochemistry, University of California, Irvine, CA 92697-3900, USA. [2]Department of Chemistry, Virginia Commonwealth University, Richmond, VA 23284-2006, USA.

Correspondence: Thomas L Poulos
E-mail: poulos@uci.edu

Key words: chloroperoxidase, crystallography, cytochrome P450, molecular dynamics, peroxidase

Received: **8 June 1998**
Revisions requested: **7 July 1998**
Revisions received: **21 July 1998**
Accepted: **21 July 1998**

Published: **18 August 1998**

Chemistry & Biology September 1998, **5**:461–473
http://biomednet.com/elecref/1074552100500461

 ISSN 1074-5521

Introduction

Chloroperoxidase (CPO) is one of the most diverse of the known heme enzyme catalysts. In addition to its biological function as a peroxide-dependent chlorinating enzyme, CPO also catalyzes reactions characteristic of traditional heme peroxidases, catalase, and cytochromes P450 [1]:

Halogenation (normal function) $RH + H_2O_2 + Cl^- + H+ \rightarrow R–Cl + 2H_2O$

Dehydrogenation (heme peroxidases) $2RH + H_2O_2 \rightarrow R–R + 2H_2O$

H_2O_2 decomposition (catalase) $2H_2O_2 \rightarrow O_2 + 2H_2O$

Oxygen insertion (P450s) $R + H_2O_2 \rightarrow R–O + H_2O$

Our recent structure determination of CPO has provided some insights into how CPO can carry out these diverse reactions [2]. Even though CPO folds into a unique structure that does not resemble either a peroxidase or a P450, CPO does share certain important structural features with both enzymes. For example, like P450, CPO has a cysteine-thiolate group as the proximal heme ligand. Moreover, the local hydrogen-bonding environment involving the cysteine sulfur is the same in both P450s and CPO. As in heme peroxidases, but unlike P450s, the distal heme surface that forms the peroxide-binding site in CPO is polar. The acid–base catalytic group that participates in the peroxide O–O bond cleavage mechanism, however, is not a histidine residue as in traditional peroxidase, but a glutamate residue.

A very striking difference between peroxidases and P450s is access to the heme center. In peroxidases, and probably in P450s, a high redox potential ferryl center, $Fe^{4+}=O$, is formed during the catalytic cycle. In peroxidases, the protein prevents direct access to this center, thereby restricting substrate–protein interactions at the heme edge [3]. As a result, aromatic organic substrates deliver electrons to the heme edge resulting in aromatic radicals. P450s, however, have a deep active-site pocket directly adjacent to the ferryl center that enables the protein to hold the substrate in place for stereoselective

Figure 1

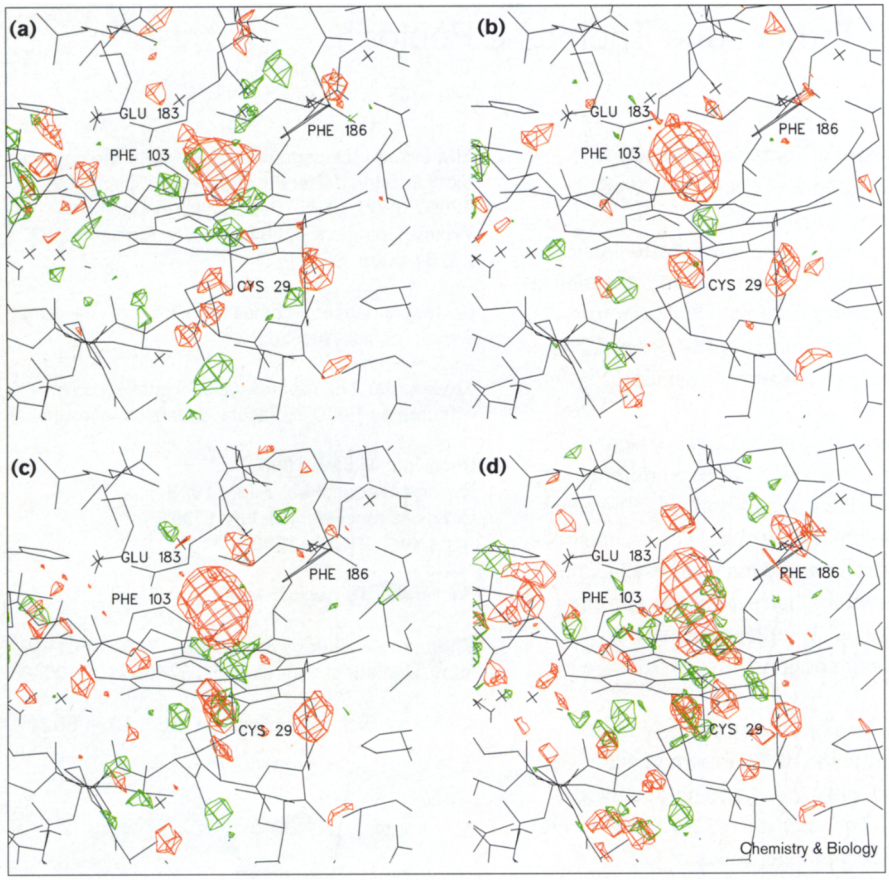

Fo–Fc difference Fourier maps with phases obtained from the unliganded native structure of CPO–ligand complexes near the heme region. **(a)** ferrous CPO–CO (pH 6.0), **(b)** ferrous CPO–NO (pH 6.0), **(c)** ferric CPO–CN (pH 6.0) and **(d)** ferric CPO–SCN (pH 3.0) complex. All the maps are contoured at ±3 σ (red, positive; green, negative) with the native CPO model superimposed. The maps were calculated using the native model structure factors and experimentally observed structure-factor amplitudes for the complexes This figure was made using SETOR [34].

and regioselective hydroxylation [4]. The CPO structure reveals that substrate access is more similar to P450s in that there is a shallow hydrophobic depression over the distal surface above the ferryl center. This appears to be the most likely place for known hydrophobic substrates to bind.

A remarkable feature of CPO is its ability to catalyze enantioselective epoxidation [5] and sulfoxidation reactions [6]. Even in the traditional heme-peroxidase reaction where aromatic radicals are formed, CPO is highly stereoselective, a feature not shared by other peroxidases. This has made CPO an attractive enzymatic system for useful enantioselective oxidation reactions. The obvious crystallographic approach to study these reactions is to form complexes between the enzyme and substrates and use difference Fourier methods to work out the structures. Thus far, it has proven possible to form complexes between CPO crystals and various diatomic and triatomic ligands that mimic peroxide binding. Diffusion of small organic substrates into the crystals has not yet been successful, however. As a result, we have initiated modeling studies and energetic analysis to assess possible binding modes of various organic substrates to provide some insight into how CPO gives enantioselective epoxides. Here, we present experimental crystallographic results on the binding of ligands to the distal heme pocket of CPO and modeling studies on the binding of a known substrate, *cis*-β-methylstyrene, to the CPO active site that provides a possible explanation for the favored conversion of this substrate to the 1*S*,2*R* epoxide.

Results and discussion

Initial difference Fouriers and refinement of ligand complexes

Several attempts were made to form stable ligand complexes with a variety of monatomic, diatomic, and triatomic ligands that can potentially coordinate to the heme iron. Those that succeeded in forming stable Fe–X complexes in the crystalline state were Fe^{2+}–CO, Fe^{2+}–NO, Fe^{3+}–CN and Fe^{3+}–SCN. All complexes formed at pH 6.0 except for the SCN complex, which appeared in difference Fourier maps only when the pH was lowered to 3.0 (Figure 1).

The difference electron density maps exhibited features only in the vicinity of ligand binding. Somewhat surprisingly, Glu183, which is situated directly adjacent to the bound ligands, as well as other neighboring residues, has

Table 1

Crystallographic refinement summary.

Complex	CPO–CO	CPO–NO	CPO–CN	CPO–SCN
Resolution range (Å)	8.0–2.1	8.0–1.9	8.0–1.9	8.0–1.9
Reflections measured	20,279	27,400	29,057	27,662
Reflections used	17,202	23,633	26,967	25,717
$F > 2\sigma(F)$				
R-factor	0.207	0.186	0.190	0.185
Rms deviation				
Bond lengths (Å)	0.011	0.009	0.010	0.008
Bond angles (°)	1.610	1.528	1.578	1.432

no difference electron density, indicating that no movement of active-site residues is required in order to accommodate even triatomic ligands.

The appropriate ligands were modeled and the protein–ligand models were refined, using conventional conjugate-gradient positional and isotropic *B*-factor refinements. No major manual adjustments of the models were needed during the refinement. Except for the CPO–SCN model, all the ligands exhibited low crystallographic *B*-factors comparable to those of protein atoms. The temperature factors for SCN atoms, when refined with unit occupancy, were relatively higher, suggesting lower occupancy due to the slow loss of SCN during the data collection. It seems likely that, even at pH 3.0, SCN does not form as stable a complex as do the other diatomic ligands. In order to remove bias on the various ligand-bonding parameters, the refinement was carried out without restraining the Fe–ligand distances and the electrostatic and van der Waals energy functions were removed in the final round of X-PLOR refinement. The differences in the ligand geometry before and after this step are not significant in any of the four structures (data not shown). The final refinement statistics for all the four complexes are provided in Table 1.

Protein structure

In Figure 2, the refined structures of ferrous CPO–CO and CPO–NO, and ferric CPO–CN and CPO–SCN are shown superimposed with the native ferric CPO structure. The CPO–ligand complex structures are indistinguishable from the native structure. Both the proximal ligand, Cys29, and the distal residues, most notably the acid–base catalytic residue, Glu183, are unperturbed by ligand binding. In addition, the hydrogen bond between His105 and Glu183 remains intact and unperturbed (Figures 3 and 4). This is in sharp contrast to significant movement of sidechains both in the proximal and distal regions in the crystal structures of protein–ligand complexes of other hemoproteins, such as cytochrome c peroxidase (CcP) [7], *Arthromyces ramosus* peroxidase (ARP) [8], cytochrome $P450_{CAM}$ [9] and myoglobin [10]. All the ligands, apart from forming exogenous ligands with heme Fe, also interact with the Glu183 sidechain carboxylate via hydrogen bonding or electrostatic interactions (Figures 3 and 4; Table 2).

Ligand and heme geometry

The geometrical parameters of the heme-bound endogenous and exogenous ligands from the final unrestrained refinements are given in Table 3. In all four CPO–ligand complexes, the Fe–X–Y bonds are not linear and all the ligands bind in a bent configuration (Figures 2 and 3; Table 3). The maximum bend is in the ferrous CPO–CO complex in which the Fe–C–O angle is 138°. In the case of the $P450_{CAM}$ and cytochrome c peroxidase structures, the Fe–C–O unit is in a bent configuration, but the angle is close to linear, about 166° in $P450_{CAM}$ [9] and 168° in CcP [7]. The direction of the bend is towards Glu183 in CPO, which places the CO oxygen 3.2 Å from Glu183. In the other ferrous complex, CPO–NO, the Fe–N–O angle is about 157°, which is significantly higher than the

Figure 2

Stereoscopic view of refined structures of native CPO and CPO–ligand complexes superimposed near the heme region. Native CPO, gray; CPO–CO, green; CPO–NO, yellow; CPO–CN, red; and CPO–SCN, blue. This figure was made using SETOR [34].

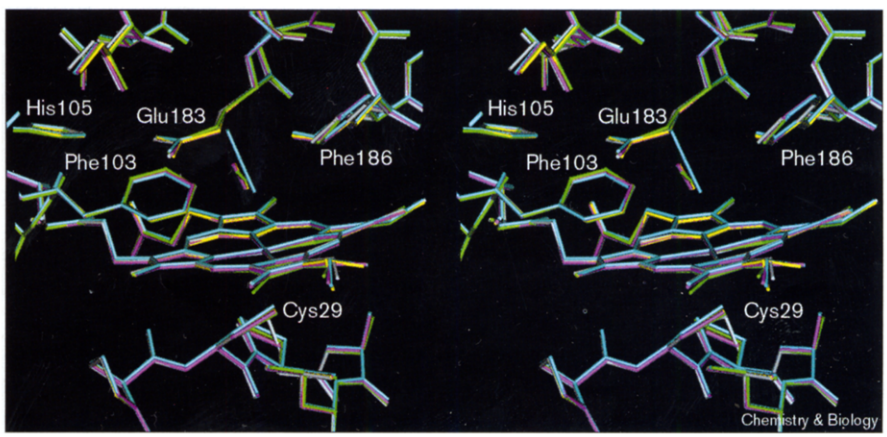

Figure 3

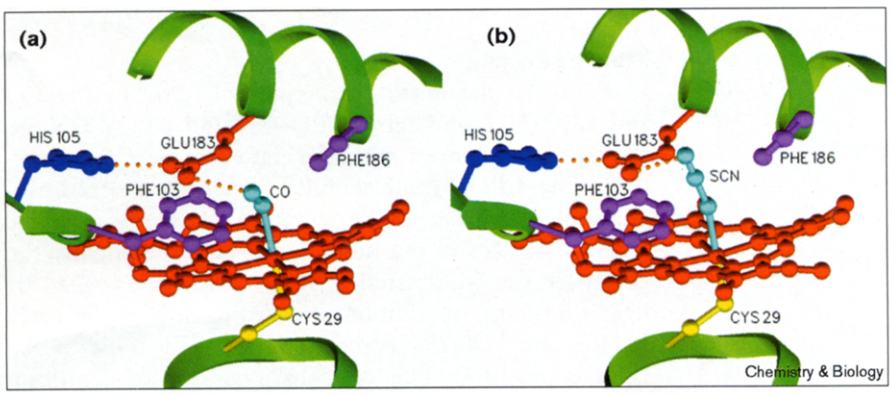

Active-site structures in CPO–ligand complexes. **(a)** The CPO–CO complex and **(b)** the CPO–SCN complex. The hydrogen bond between Glu183 and His105 is conserved in all the complexes and is similar to the native CPO structure. Additionally, the terminal atoms in the ligands also form hydrogen bonds with Glu183. This figure was made using SETOR [34].

Fe–C–O angle. The interaction of the NO oxygen with Glu183 is stronger in this case, with a distance of 2.9 Å. In the ferrous CPO–ligand complexes, CO and NO donate an electron to the reduced iron and the terminal oxygen atoms carry a partial positive charge. As at pH 6.0, Glu183 should be in the anionic carboxylate state, it would appear that the primary mode of interaction between Glu183 and CO or NO is electrostatic and not hydrogen bonding.

In the ferric complexes the ligands bind in a near-linear configuration. The Fe–X–Y angles in both ferric complexes are comparable — about 166° in the CPO–SCN complex and about 161° in CPO–CN. As in the other complexes, the ligands contact Glu183 (Figure 4). One major difference between CN and SCN is that CN binds over a wide range of pHs, whereas SCN binds only at low pH [11]. At pH 6.0, the weakly acidic CN (pK_a 9.14) should be protonated so HCN coordinated to the heme iron serves as a hydrogen-bond donor to Glu183. On the other hand, the strongly acidic SCN (pK_a –1.9) cannot bind to iron at high pH without a significant movement of Glu183 due to the electrostatic repulsion. SCN therefore binds only at low pH, where Glu183 is protonated, resulting in hydrogen-bonding interactions. In the SCN complex structure at pH 3.0, Glu183 therefore acts as a hydrogen-bond donor, whereas in the HCN complex Glu183 is a hydrogen-bond acceptor. It is also quite interesting that the CPO active-site structure is insensitive to structural changes in the range of pH 3.0–6.0, which further underscores the rigid CPO active-site architecture.

The displacement of iron into the heme plane in CPO–CO, CPO–NO and CPO–CN complexes agrees well with the low-spin nature of heme in these complexes (Table 3). In the low-spin CPO–SCN complex, however, the displacement is 0.10 Å, close to the 0.14 Å value for high-spin native CPO. A similar lack of correlation between the spin-state and iron position relative to the porphyrin plane was also found in CcP–ligand complexes [7]. This ambiguity is also reflected in the shorter Fe–S distance (2.2 Å) in the CPO–SCN complex compared to the other complexes (> 2.3 Å). Similarly, the Fe–X distance in the CPO–SCN complex is relatively short (2.35 Å) compared to the distance in the other complexes (> 2.4 Å). The Fe–S distance of 2.41 Å in the ferrous CPO–CO complex correlates very well with the corresponding distance of 2.35–2.41 Å in the CO–camphor–$P450_{CAM}$ crystal structure [9], even though in the native ferric states the distances are different, 2.3 Å in CPO and 2.2 Å in $P450_{CAM}$. Also, the Fe–C distances in the two structures are significantly different —about 2.5 Å in the CPO–CO structure and 2.0 Å in CO–camphor–$P450_{CAM}$.

Mechanistic implications

Perhaps the most important and unexpected observations from these structures is the total lack of change in the position of Glu183 and surrounding residues when ligands bind or the pH is lowered from 6.0 to 3.0 (Figure 2). Such rigidity explains the discrimination of ligands on the basis of size. The space between Fe and Glu183 is too large to bind a monatomic ligand, such as a halide ion, to interact strongly with Glu183. In contrast, the distal residues in CcP move to accommodate ligands [7]. Depending upon the size and charge of the ligand, the distal residue, Arg48 in CcP, moves towards or away from the peroxide-binding pocket. In the CcP–F complex, the guanidinium group of Arg48 moves about 2.5 Å towards the fluoride ligand in order to maximize interactions. In contrast, in the diatomic CcP–NO complex Arg48 moves away from the ligand 0.6 Å. The distal acid–base catalyst in CcP, His52, also moves 0.2–0.5 Å in the various complexes. This flexibility explains the role of arginine in forming and stabilizing compound I in CcP. Arg48 can move away from the ligand in the ferric–peroxide complex but can move towards the ligand in compound I such that Arg48 directly interacts with Fe^{4+}=O oxygen atom [12,13].

Figure 4

Schematic representation of chemical structures and distances involving the active site Glu183 residue: **(a)** native CPO, **(b)** CPO–CO, **(c)** CPO-NO, **(d)** CPO–CN and **(e)** CPO–SCN.

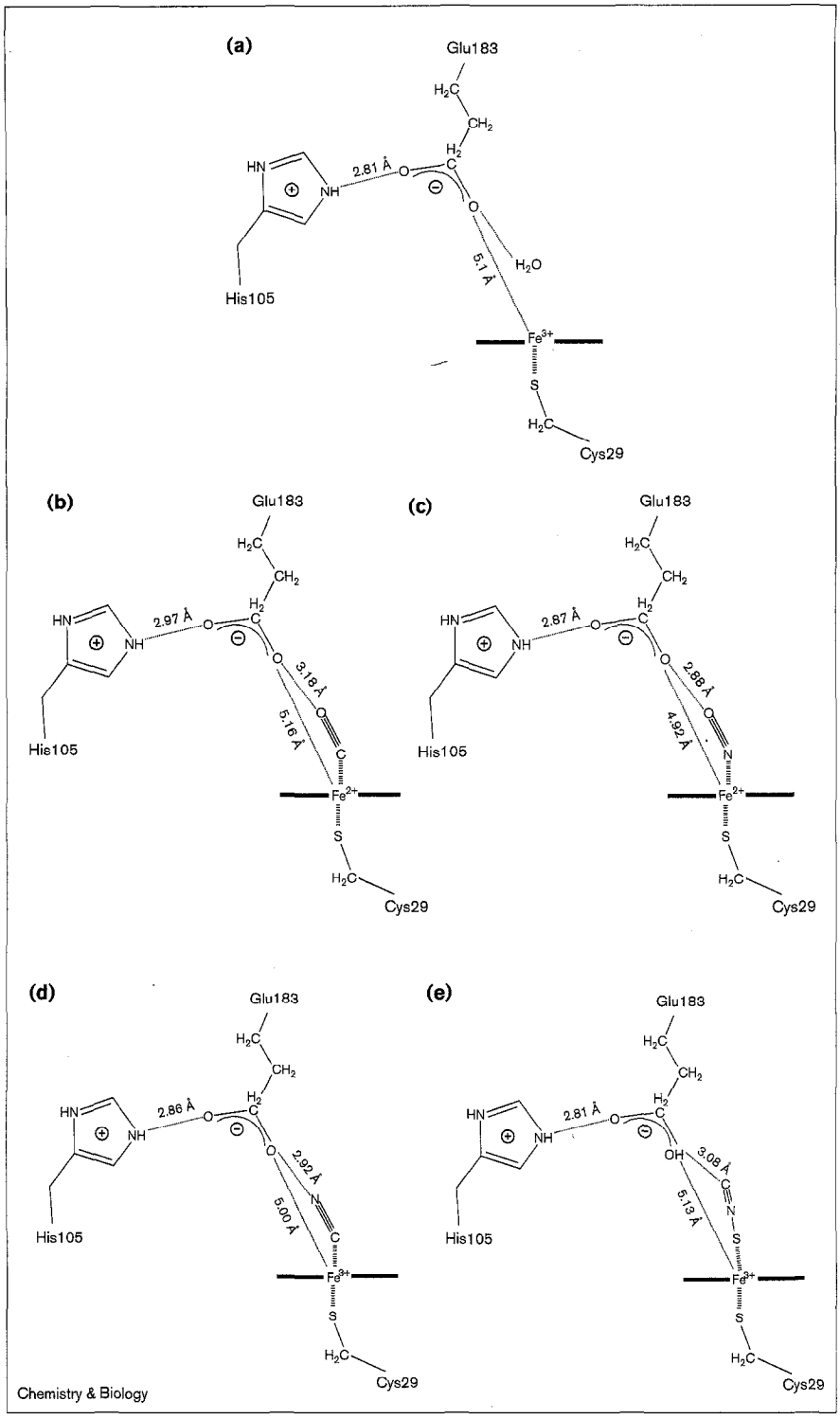

The present studies suggest that Glu183 can carry out its catalytic functions with very little movement. A possible mode of catalysis, similar to that proposed earlier [14], is outlined in Figure 5. In the native CPO structure, the peroxide-binding pocket is occupied by a water molecule that is 3.2 Å from the iron and forms a hydrogen bond with the carboxylate group of Glu183 (**1**). The incoming hydrogen peroxide substrate displaces the distal water and Glu183 abstracts a peroxide proton (**2**). The singly ionized hydrogen peroxide covalently binds to iron (**3**) to

Table 2

Distances of Glu183 from ligands, His105 and Fe in the complexes.

Structure	Glu183–ligand (Å)	Glu183–Fe (Å)	Glu183–His105 (Å)
Native		5.10	2.81
CPO–CO	3.18	5.16	2.97
CPO–NO	2.88	4.92	2.87
CPO–CN	2.92	5.00	2.86
CPO–SCN	3.08	5.13	2.81

Table 3

Geometrical parameters of heme and Fe–ligands.

Structure	S–Fe distance (Å)	L–Fe distance (Å)	Fe to pyrrole N plane (Å)	bend of Fe–X–Y angle (°)
CPO (native)	2.30		0.14	
CPO–CO	2.41	2.47	0.02	137.6
CPO–NO	2.31	2.55	0.08	157.2
CPO–CN	2.35	2.58	0.05	161.4
CPO–SCN	2.16	2.36	0.10	166.2

L, ligand.

form a short-lived intermediate. This intermediate complex brings the terminal oxygen atom of the activated peroxide species closer to Glu183 (**4**) to form a strong hydrogen bond, similar to the situation with diatomic ligand complexes. This facilitates the subsequent proton delivery to the terminal oxygen atom by Glu183 resulting in the heterolytic cleavage of the O–O bond of the peroxide. The low pH optimum of CPO near the pK_a of carboxylates (pH 3.0) [15] might be required so that Glu183 can serve both as a proton acceptor and donor during the heterolytic cleavage of the peroxide O–O bond. One oxygen atom with only six valence electrons remains linked to the iron, which rearranges to give the compound I oxoferryl center (Fe^{4+}=O) and porphyrin π cation radical [16,17] found in other heme peroxidases. Thus, Glu183 serves as the acid–base catalyst facilitating proton transfer from one oxygen to the other in the same peroxide molecule [14]. This mechanism is basically the same as that proposed initially for CcP [18] except that Glu183 operates as the acid–base catalyst rather than histidine. Unlike the CcP compound I, however, CPO compound I is short lived and relatively unstable [19], partly due to the rigid nature of the active site and the inability of Glu183 to swing in and form a stabilizing hydrogen bond as arginine does in CcP [12,13]. This inference is drawn from the fact that CPO fails to form stable complexes with monatomic ligands, unlike CcP [7] and ARP [8]. Addition of Cl^- results in the rapid formation of a postulated Fe–OCl adduct (**6**). It has been thought that this species is directly responsible for the transfer of halides to halide-accepting substrates such as monochlorodimedone [20]. This would presumably require direct binding of such substrates close to the oxoferryl center. No halide-accepting substrate is yet known to form a Michaelis–Menten complex with CPO, however [1]. Other studies have shown that CPO–OCl releases HOCl or Cl_2, depending upon the concentration of Cl^- in the reaction [21,22]. Moreover, CPO performs chlorination below pH 4.0. At low pH, the iron-bound oxy-chloride species is thought to be protonated by the hydronium ion (**7**), resulting in the formation of a Fe–HOCl adduct (**8**). Subsequent release of HOCl returns the enzyme to its resting state (**1**). In the absence of halides, the unstable compound I oxidizes small organic substrates reminiscent of peroxidases or undergoes a fast two-electron reduction similar to catalase returning to the resting state (**1**). In addition to protonating the putative Fe–OCl intermediate, the low pH optimum of CPO might also be related to the high redox potential required to oxidize Cl^-. The redox potential of most heme peroxidases tends to increase with decreasing pH [23]. If this trend is followed in CPO compound I, then compound I should be a more potent oxidant at low pH. Hence, the low pH optimum of CPO might be required so that CPO compound I has a high enough redox potential to oxidize Cl^-, a reaction that traditional heme peroxidases operating closer to neutral pH cannot carry out. This, in turn, requires an acid–base catalyst whose pK_a matches the required pH for Cl^- oxidation. This is one possible reason why CPO utilizes a carboxylate acid–base catalyst rather than a histidine residue.

Modeling CPO's P450-like chemistry

The discussion thus far helps to understand the chloroperoxidase activity of CPO. CPO, however, also catalyzes P450-like reactions. For example, Allain *et al.* [5] found that CPO is able to convert a variety of allelic compounds to epoxides, some with a very high level of enantioselectivity. Our goal was to see if we could provide a structural basis for this selectivity. We chose to use *cis*-β-methylstyrene as a substrate because this compound is converted to 1*S*,2*R* epoxide with 96% enantioselectivity. Unfortunately, attempts to diffuse known substrates into CPO crystals have not yet yielded interpretable difference Fouriers. We have therefore attempted to gain some insight into how CPO carries out such reactions using molecular modeling methods. We were encouraged to pursue this line of investigation because of the success of Fruetel *et al.* [24] in correctly modeling the P450-catalyzed epoxidation of *cis*-β-methylstyrene.

Figure 5

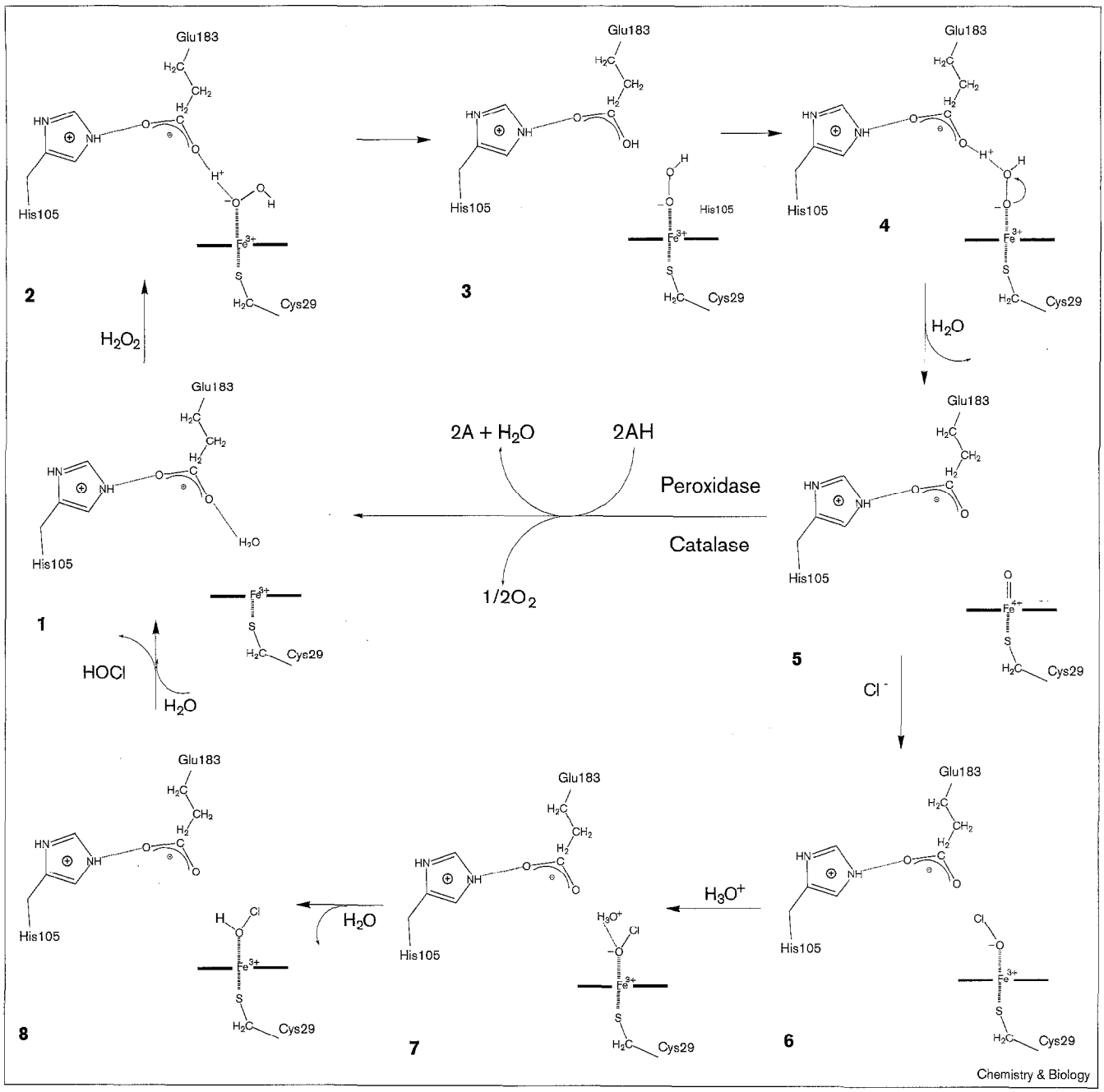

Schematic representation of the proposed CPO catalytic cycle.

The protein model used for docking the substrate in place was the crystal structure after exhaustive energy minimization. As the functionally relevant form of CPO contains an oxoferryl center, the heme parameters used for energy minimization and molecular dynamics were those for an oxoferryl heme [25]. The location of the binding pocket is shown in Figure 6. This pocket forms an opening, just above the heme, that contains five ordered solvent molecules. In docking studies we assume that a hydrophobic substrate will displace these solvent molecules in favor of substrate–protein nonbonded interactions. The substrate can adopt a number of orientations, all equally favorable, within this pocket. The double bond must interact with the oxoferryl center in order to form the epoxide, however. We therefore held the distance between the two ethylene carbon atoms and the oxoferryl oxygen atom to 4 Å, which severely restricts the number of possible binding orientations.

Figure 6

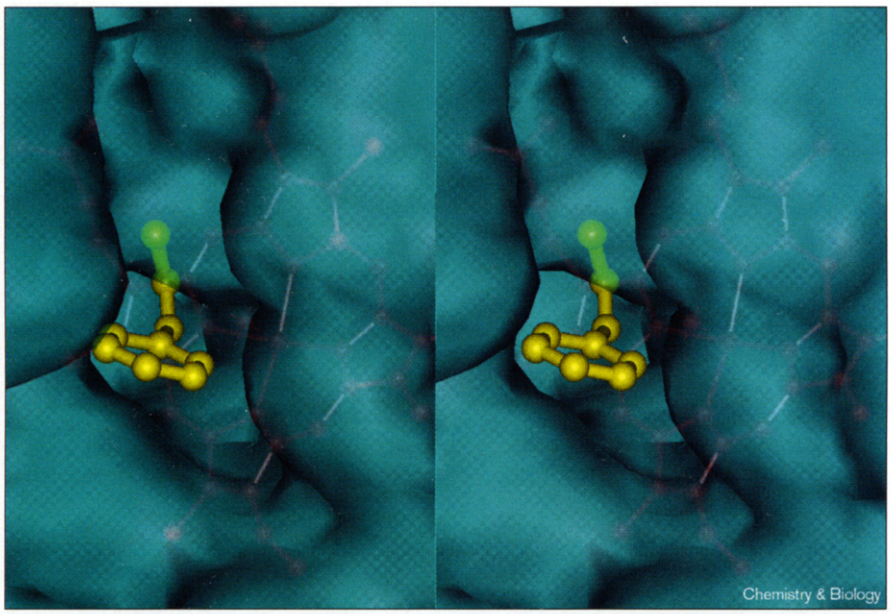

Stereoscopic view of the substrate binding pocket in CPO. This is a semi-transparent molecular surface diagram showing the docked *cis*-β-methylstyrene (yellow) in the substrate pocket just above the heme (red).

Two models were constructed, one corresponding to the orientation that will give the 1*S*,2*R* epoxide and the second to the 1*R*,2*S* epoxide. The primary difference between the two epoxides is in the position of the substrate methyl group relative to the remainder of the substrate. After manually docking, the two structures were energy minimized. During the minimization, the distances between the two methylene carbons and oxoferryl oxygen atom was constrained between 3.5 and 4.0 Å. The resulting minimized structures in the vicinity of the active site are shown in Figure 7. Using the Discover software, the interaction energy between the substrate in the two configurations was examined and is summarized in Figure 8. Overall, the two configurations interact with the surrounding protein with nearly the same favorable energy. There is a large difference in the interactions when fragments of the substrate are examined, however. For example, the methyl group experiences a much more favorable interaction in the 1*S*,2*R* configuration than in the 1*R*,2*S* orientation, due to a more favorable electrostatic interaction between the substrate methyl group and Glu183. The favorable electrostatic component is caused by the interaction between the methyl protons and Glu183 carboxyl group.

This same procedure was repeated, except that the epoxides of 1*S*,2*R* and 1*R*,2*S* isomers were modeled into the active site. We assume here that, at some point along the reaction trajectory, the epoxide will form with the epoxide oxygen atom still interacting with the heme iron atom, providing another level of discrimination between the epoxide isomers. In this case, the distance between the epoxide oxygen and heme iron atom was restrained in the range of 2.5–3.0 Å during the energy minimization. The static energy-minimized structures exhibit no significant differences in interactions with neighboring protein groups. There is a small preference for the methyl group in the 1*S*,2*R* configuration, but this is offset by more favorable interactions with other regions of the *cis*-β-methylstyrene molecule in the 1*R*,2*S* isomer, such as the benzene ring.

These results indicate that the orientation of the methyl group favoring the experimentally observed 1*S*,2*R* configuration also is energetically favored in the substrate, *cis*-β-methylstyrene. A more stringent test is to see how the two orientations behave during a molecular dynamics simulation. All four minimized structures were therefore subjected to a 110–120 ps molecular dynamics simulation. For the simulations, distances between substrate atoms and the oxoferryl oxygen atom were not restrained or constrained. Examination of the trajectories in a graphics 'movie' mode clearly shows that the double bond in the 1*S*,2*R* orientation remains closer to the oxoferryl oxygen atom and in the correct orientation for reaction during the simulation. This is graphically represented in Figure 9. In the 1*R*,2*S* orientation, the substrate immediately adopts a position 8–9 Å from the oxoferryl oxygen atom whereas, for most of the trajectory, the 1*S*,2*R* orientation stays within 5–6 Å of the oxoferryl oxygen atom. Also shown in Figure 9 are the average structures. Beginning with substrate docked in the 1*R*,2*S* orientation, the substrate flips over, which moves the double bond too far away and in the wrong

Figure 7

Stereo views of the energy-minimized complexes formed between *cis*-β-methylstyrene and CPO. The top view is oriented to give the 1*S*,2*R* epoxide, whereas the bottom model is for the 1*R*,2*S* epoxide. This figure was made using MOLSCRIPT [35].

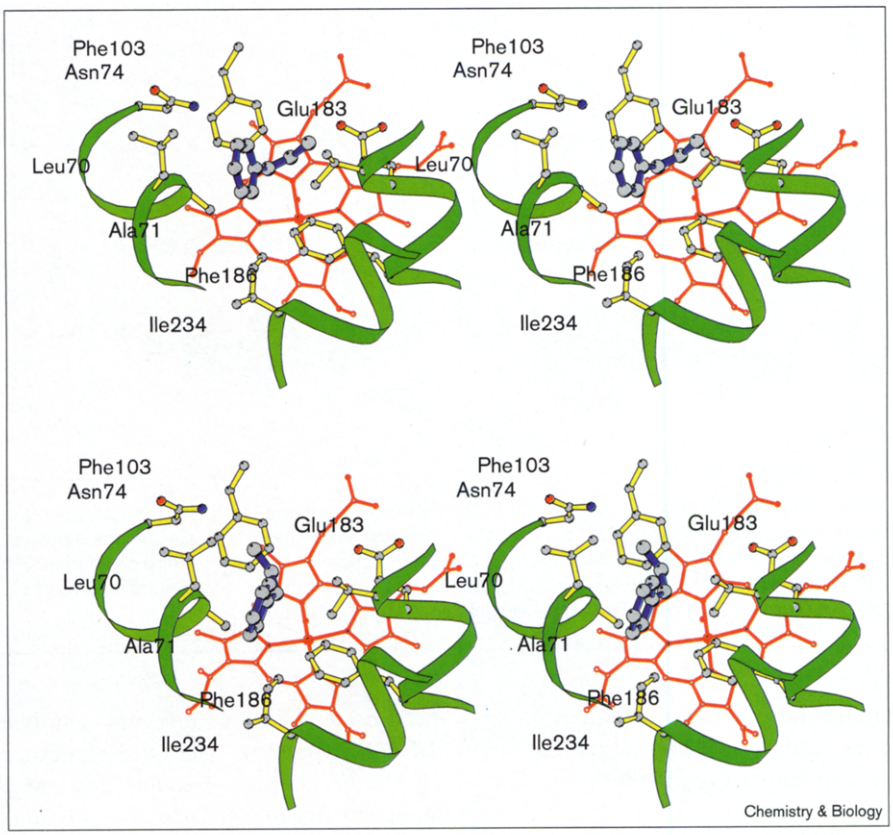

orientation for reaction with the oxoferryl oxygen atom. This indicates that, if the substrate approached the active site in the 1*R*,2*S* orientation, it does not spend a significant fraction of time in a position consistent with epoxide formation. In sharp contrast, the 1*S*,2*R* docked conformation remains in the correct orientation and much closer to the oxoferryl oxygen atom throughout most of the simulation. The orientation that would give the experimentally favored 1*S*,2*R* enantiomer is therefore favored, on the basis of both static energetic analysis and

Figure 8

Energetic analysis of the various configurations for both the substrate and epoxide product. After energy minimization of each complex, the detailed energetic interactions between the various groups and nearby protein atoms were calculated.

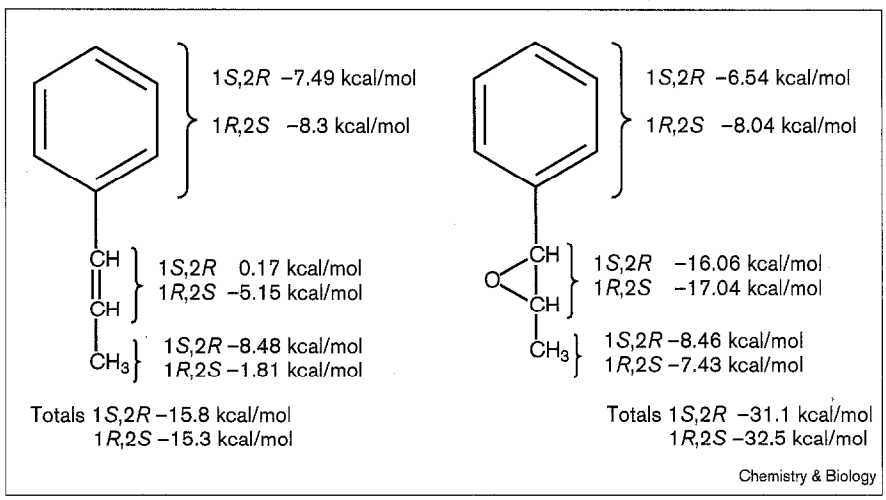

Figure 9

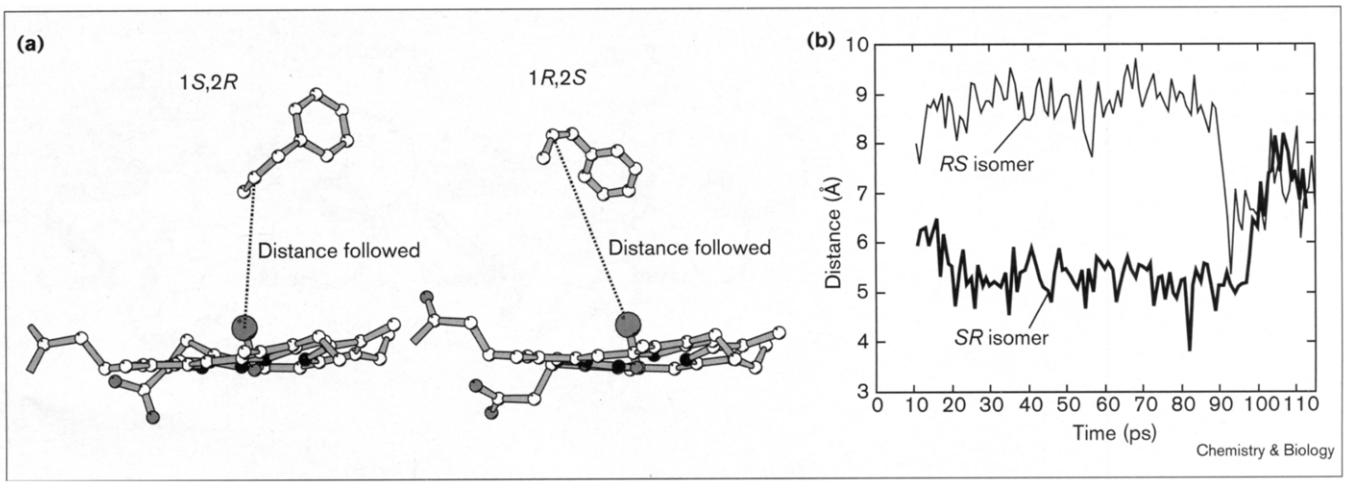

Results of a molecular dynamics simulation for the two orientations of the *cis*-β-methylstyrene substrate. The starting models were the energy-minimized structures based on the 1*S*,2*R* orientation or the 1*R*,2*S* orientation. The energy-minimized structures had the distance between the epoxide hydrogen atoms and heme iron held constant. No restraints were employed during the molecular dynamics simulations, however. The models shown are averages taken over the entire simulation. The plot is the indicated distance as a function of simulation time. This figure was made using MOLSCRIPT [35].

molecular dynamics. Simulations with the product epoxides lead to similar results. In the 1*S*,2*R* configuration, the epoxide oxygen atom remains closer to the heme iron atom (Figure 10). In the 1*R*,2*S* configuration, the product epoxide flips over, with the oxygen atom pointing away from the heme iron atom, giving a much longer distance between the epoxide oxygen and heme iron atoms.

Significance

For the past three decades, chloroperoxidase (CPO) has received wide attention as the most versatile heme enzyme catalyst. The present studies involving the crystal structures of CPO–ligand complexes and molecular dynamics of CPO–substrate/product complexes provide new insights towards an understanding of CPO catalysis. The rigid active-site architecture, as revealed by the CPO–ligand complex structures, explains the possible mode of compound I formation, as well as a structural basis for the discrimination of ligand binding on the basis of the size and pK_a of the ligand. A possible basis for the relative instability of CPO compound I is the inability of the rigid Glu183 acid–base catalyst to

Figure 10

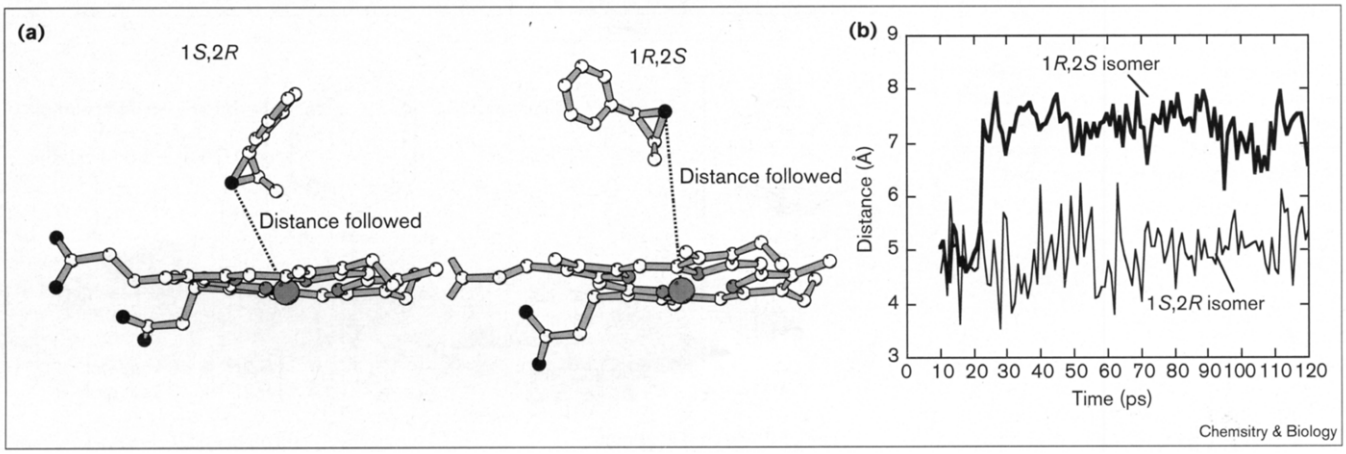

Results of a molecular dynamics simulation for the two orientations of the epoxide product (the details of the simulation are the same as in Figure 9). This figure was made using MOLSCRIPT [35].

stabilize the oxoferryl species, resulting in a highly reactive compound I intermediate capable of oxidizing Cl^- at low pH. The energetics of CPO–substrate/product complexes with *cis*-β-methylstyrene and the corresponding epoxides in two enantiomeric configurations provide theoretical support for the experimentally observed enantioselective epoxidation of styrenes, a P450-type reaction. This type of information provides a basis for the development of CPO mutants designed to catalyze stereoselective oxidations of interest, an important goal in synthetic organic chemistry.

Materials and methods

Crystallization

CPO was produced from *Caldariomyces fumago* following the procedures described by Blanke *et al.* [26]. CPO crystallizes in two space groups, $P2_12_12_1$ (P-form) and $C222_1$ (C-form), under slightly different conditions [27]. Crystals of the P-form diffract to higher resolution and are more stable in X-ray beam. P-form CPO crystals were grown using the hanging drop vapor diffusion method. The reservoir contained 30% polyethylene glycol 6000 (PEG 6000) and 10 mM potassium phosphate buffer, pH 6.0. The drops were made up of 5 µl of 10 mg/ml CPO in 50 mM potassium phosphate buffer, pH 3.7 and 5 µl of the reservoir solutions. Larger single crystals were grown using microseeding and macroseeding procedures [28]. The crystals grown using these methods diffracted to better than 2.0 Å resolution. The crystals were harvested and manipulated in an artificial mother liquor containing only 30% PEG 6000.

Preparation of complexes

Ferrous complexes of CPO–CO and CPO–NO were formed by reducing the crystals using sodium dithionite. About 2.5 ml of artificial mother liquor in a glass vial was purged with N_2 gas for 15–20 min. This solution was bubbled with CO gas for 30–40 min and about 3 mg of sodium dithionite grains were added. A large diffraction quality crystal was dropped into the vial and kept sealed air-tight for 2 h. The change in the color of the crystal from brownish red to bright red indicated the formation of CO adduct. The crystal was mounted in a glass capillary flushed with CO. A freshly prepared mother liquor treated with sodium dithionite and saturated with CO was used for mounting the crystal with plugs of the same mother liquor on either side of the crystal and the ends sealed. The CPO–NO complex was prepared following Yonetani *et al.* [29]. 2.5 ml of 30% PEG 6000 was purged with N_2 for 15–20 min. Sodium dithionite (3 mg) and 2 mg of sodium nitrite were added to the solution (sodium nitrite liberates NO in solution). A few good diffraction quality crystals were dropped in the vial and sealed air-tight. The crystals were soaked for 2 h in the dark and mounted in a glass capillary using a freshly prepared mother liquor following the same procedure as in the case of CPO–CO.

Preparation of ferric CPO–CN complex was straightforward and the complex was stable. On the other hand, ferric CPO–SCN complex preparation proved to be difficult and the complex was unstable. To prepare a CPO–CN complex, a diffraction quality crystal grown at pH 6.0 was soaked in the artificial mother liquor containing 2 mM KCN overnight. High pH crystals did not form a complex with SCN so low pH crystals grown at pH 3.0 were used for this experiment. As the crystals were unstable in the artificial mother liquor buffered with potassium phosphate, a soaking strategy described by David [30] was followed. 2 µl droplets of mother liquor at pH 3.0 plus 40 mM potassium thiocyanate were placed around the macroseeded crystal drop and equilibrated against the reservoir solution for 1–2 d. A few droplets of KSCN solution was merged with the parent drop containing the crystal such that the final concentration of KSCN in the drop was between 2 and 4 mM. The crystal soaked overnight using this method was stable and used for data collection.

Table 4

Crystallographic data collection summary.

Complex	CPO–CO	CPO–NO	CPO–CN	CPO–SCN
Data observed	72,153	88,904	142,388	107,437
Number of unique reflections	19,899	26,746	31,271	28,847
$^1R_{iso}$ (%)	11.5	6.70	4.50	9.30
R_{sym} (%)	10.52	10.04	7.92	5.5
Highest resolution (Å)	2.2	2.0	1.9	1.9
I/σ(I) at highest resolution	1.2	1.0	1.2	2.7
Completeness (%)				
Overall	98	99	99	93
Highest resolution shell	96	97	96	

$^1R_{iso}$ = scaling R factor between native and liganded data set; R_{sym} = scaling R factor between symmetry related and multiply measured reflections.

Data collection and refinement

Diffraction data were obtained from a single crystal for each complex. The X-ray data sets of CPO complexes with CO, NO and CN were collected using Siemens area detector system and Siemens rotating anode X-ray source equipped with short Supper mirror optics. The complete data sets were collected over 24–36 h. F_o(complex)–F_c(native) electron density maps were computed using partial data collected at different time periods indicated difference density for the ligand. Ferrous complex crystals with CO and NO appeared to lose the ligands if the data collection was extended beyond 2 d. The data were integrated, reduced and scaled using XENGEN software package [31]. The CPO–SCN complex data were collected using an Raxis IV imaging plate system on a Rigaku rotating anode X-ray source equipped with Yale mirrors. The relatively higher operating power and the imaging plate system insured faster data collection for this unstable complex. A complete data set was obtained in 12 h. The data were integrated with the DENZO software package and scaled using SCALEPACK [32] The data collection summary for all complexes is provided in Table 4.

Crystallographic refinement and electron-density-map calculations were carried out using X-PLOR [33]. The ligand models were built in the difference electron-density maps and parameter-restrained positional refinement was carried out for each complex. The bond and angular parameters for the ligand molecules and Fe–ligand complexes were gathered from the crystal-structure data of small molecular complexes. Fe^{2+}, in the case of ferrous complexes and Fe^{3+} in ferric complexes were treated as separate groups free from porphyrin. The Fe–ligand distances for all the six ligands were restrained with smaller force constants. The initial occupancies and temperature factors (*B*-factor) for the ligand atoms were set at 1.0 and 15.0 Å respectively. The $2F_o–F_c$ and $F_o–F_c$ maps were calculated after each refinement step and examined. The solvent structure in the active site was rebuilt. Also, during the course of refinement and model building, the maps were examined in other regions, and a few sugar and solvent molecules, which had poorly defined electron density and high *B*-factors, were removed from the model. This iterative process was continued until the crystallographic *R*-factor converged and the difference Fourier maps showed no residual electron density in the active site region. During the initial stages, *B*-factors were refined followed by positional refinement.

Molecular modeling

Molecular dynamics and energy minimization calculations were carried out using Discover (version 2.9) from Biosym Technologies. The overall procedures used were very similar to those used by Fruetel *et al.* [24] in modeling P450-catalyzed epoxidation reactions. The forcefield parameters were taken from the standard library provided by Biosym (consistent valence forcefield) with the exception of the heme and cysteine thiolate ligand parameters. As the catalytically relevant form of the heme is the oxoferryl heme (Fe^{4+}=O), parameters for the oxoferryl heme were used [25]. The CPO model, which included crystallographically defined solvent molecules, first was energy minimized. Nonbonded interactions were set to zero at a cut-off distance of 13 Å with a switching function width of 2.0 Å. No cross terms were used and the dielectric was set to 1.0. As only those water molecules found in the crystal structure were included, charged amino acids were made net neutral to compensate for the effect of bulk solvent. The following protocol was used for all energy minimization runs. All hydrogen atoms were allowed to move for 1000 steps. All water molecules were allowed to move for 1000 steps. All sidechain atoms plus waters were allowed to move for 2000 steps. In these first three steps, the method of steepest descents was used. In the last step, all atoms were allowed to move until the average change in energy with respect to atomic position was less than 0.1 Kcal/Å, using the conjugate gradient method. The overall root mean square deviation of backbone atoms between the minimized and crystal structures was 0.92 Å.

The substrate was manually docked to the energy minimized structure with the distance between the two allylic H atoms held at a distance of 3.5 Å from the heme oxoferryl oxygen atom. Which epoxide is formed, 1*S*,2*R* or 1*R*,2*S*, depends primarily on the orientation of the substrate methyl group relative to the remainder of the substrate. Two orientations of the methyl group were modeled, each corresponding to one of the epoxide isomers. The benzene ring in both molecules was positioned in the same open hydrophobic pocket normally occupied by solvent molecules. These solvents were assumed to be displaced when substrates bind and hence were eliminated from the model. Both docked complexes were subjected to full conjugate gradient energy minimization except the distance between the allylic H atoms and oxoferryl oxygen atom was restrained to 3.5 Å–4.0 Å. These energy minimized structures were next used for molecular dynamics. Molecular dynamics was initiated by first assigning random velocities followed by equilibration at 300K for 10 ps. This was followed by 100–110 ps of molecular dynamics at 300K with coordinates saved every 0.5–1.0 ps. Energy minimization and molecular dynamics of the two product isomers followed the same protocol except, in this case, the distance between the epoxide oxygen and heme iron atoms was held constant at 2.5–3.5 Å during energy minimization, whereas no restraints were applied during the molecular dynamics simulations.

Acknowledgements

This work was supported by National Science Foundation Grant MCB 9405128 (to T.L.P.) and National Institutes of Health Grant GM 57042 (to J.T.). We also thank Danni Harris and Gilda Loew for providing the heme oxoferryl parameters used in the computational work.

References

1. Griffin, B.W. (1992). Chloroperoxidase: a review. In *Peroxidases in Chemistry and Biology.* (Everse, J., Everse, K.E. and Grisham, M.B., eds) Vol II, pp. 85-137, CRC Press, Boca Raton, FL, USA.
2. Sundaramoorthy, M., Terner, J. & Poulos, T.L. (1995). The crystal structure of chloroperoxidase: a heme peroxidase-cytochrome P450 functional hybrid. *Structure* **3**, 1367-1377.
3. Finzel, B.C, Poulos, T.L. & Kraut, J. (1984). Crystal structure of yeast cytochrome c peroxidase refined at 1.7 Å resolution. *J. Biol. Chem.* **259**, 13027-13036.
4. Poulos, T.L., Cupp-Vickery, J.R. & Li, H. (1995). Structural studies on prokaryotic cytochromes P450. In *Cytochrome P450: Structure, Mechanism, and Biochemistry* (Ortiz de Montellano, P.R. ed) pp.125-150. Plenum Press, New York.
5. Allain, E.J., Hager, L.P., Deng, L. & Jacobsen, E.N. (1993). Highly selective enantioselective epoxidation of disubstituted alkenes with hydrogen peroxide catalyzed by chloroperoxidase. *J. Am. Chem. Soc.* **115**, 4415-4416.
6. Colonna, S., *et al.*, & Pasta, P. (1990). Enantioselective oxidations of sulfides catalyzed by chloroperoxidase. *Biochemistry*, **29**, 10465-10468.
7. Edwards, S.L. & Poulos, T.L. (1990). Ligand binding and structural perturbations in cytochrome c peroxidase. *J. Biol. Chem.* **265**, 2588-2595.
8. Fukuyama, K., Kunishima, N., Amada, F., Kubota, T. & Matsubara, H. (1995). Crystal structures of cyanide- and triiodide-bound forms *of Arthromyces ramosus* peroxidase at different pH values. Perturbations of active site residues and their implication in enzyme catalysis. *J. Biol. Chem.* **270**, 21884-92.
9. Raag, R. & Poulos, T.L. (1989). Crystal structure of the carbon monoxide-substrate-cytochrome P450CAM ternary complex. *Biochemistry* **28**, 7586-7592.
10. Conti, E., *et al.*, & Bolognesi, M. (1993). X-ray crystal structure of ferric *Aplysia limacina* myoglobin in different liganded states. *J. Mol. Biol.* **233**, 498-508.
11. Sono, M., Dawson, J.H., Hall, K. & Hager, L.P. (1986). Ligand and halide binding properties of chloroperoxidase: peroxidase-type active site heme environment with cytochrome P-450 type endogenous axial ligand and spectroscopic properties. *Biochemistry* **25**, 347-356.
12. Edwards, S.L., Xuong, N-h., Hamlin, R.C. & Kraut, J. (1987). Crystal structure of cytochrome c peroxidase compound I. *Biochemistry* **26**, 1503-1511.
13. Fulop, V., *et al.*, & Edwards, S.L. (1994). Laue diffraction study on the structure of cytochrome c peroxidase compound I. *Structure* **2**, 201-208.
14. Wagenknecht, H-A. & Woggon, W-D. (1997). Identification of intermediates in the catalytic cycle of chloroperoxidase. *Chem. Biol.* **4**, 367-372.
15. Thomas, J.A., Morris, D.R. & Hager, L.P. (1970). Chloroperoxidase. VIII. Formation of peroxide and halide complexes and their relation to the mechanism of the halogenation reaction. *J. Biol. Chem.* **245**, 3135-3142.
16. Hewson, W.D. & Hager, L.P. (1979). Peroxidases, catalases, and chloroperoxidase. In *The Porphyrins, Part B,* (Dolphin, D. ed). Vol. 7, pp. 295-332.
17. Roberts, J.E., Hoffman, B.M., Rutter, R., & Hager, L.P. (1981). Electron-nuclear double resonance of horseradish peroxidase compound I. Detection of the porphyrin pi-cation radical. *J. Biol. Chem.* **256**, 2118-2121.
18. Poulos, T.L. & Kraut, J. (1980). The stereochemistry of peroxidase catalysis. *J. Biol. Chem.* **255**, 8199-8205.
19. Araiso, T., Rutter, R., Palcic, M.M., Hager, L.P. & Dunford, H.B. (1980). Kinetic analysis of compound I formation and the catalatic activity of chloroperoxidase. *Can. J. Biochem.* **59**, 233-236.
20. Libby, R.D., Thomas, J.A., Kaiser, L.W. & Hager, L.P. (1981). Chloroperoxidase halogenation reactions. *J. Biol. Chem.* **257**, 5030-5037.
21. Geigert, J., Neidleman, S.L. & Dalietos, D.J. (1983). Novel haloperoxidase substrates: alkynes and cyclopropanes. *J. Biol. Chem.* **258**, 2273-2277.
22. Griffin, B.W. (1983). Mechanism of halide simulated activity of chloroperoxidase. Evidence of enzymatic formation of free hypohalous acid. *Biochem. Biophys. Res. Commun.* **116**, 873-879.
23. Hayashi, Y. & Yamazaki, I. (1979). The oxidation-reduction of compound I/compound II and compound II/ferric couples of horseradish peroxidases A2 and C. *J. Biol. Chem.* **254**, 9101-9106.
24. Fruetel, J.A., Collins, J.R., Camper, D.L., Loew, G.H., Ortiz de Montellano, P.R. (1992). Calculated and experimental asbolute stereochemistry of the styrene and β-methylsytrene epoxides formed by cytochrome P450cam. *J. Am. Chem. Soc.* **114**, 6987-6993.
25. Collins, J.R., Camper, D.L. & Loew, G.H. (1991). Valproic acid metabolism by cytochrome P450: a theoretical study of stereoelectronic modulators of product distribution. *J. Am. Chem. Soc.* **113**, 2736-2743.
26. Blanke, S.R., Yi, S. & Hager, L.P. (1989). Developement of semi-continuous and continuous flow bioreactors for the high level production of chloroperoxidase. *Biotechnol. Lett.* **11**, 842-844.
27. Sundaramoorthy, M., Mauro, J.M., Sullivan, A.M., Terner, J. & Poulos, T.L. (1995). Preliminary crystallographic analysis of chloroperoxidase from *Caldariomyces fumago. Acta Crystallogr. D* **51**, 842-844.

28. Stura, E.A. & Wilson, I.A. (1991). Applications of the streak seeding technique in protein crystallization. *J. Cryst. Growth* **110**, 270-282.
29. Yonetani, T., Yamamoto, H., Erman, J.E., Leigh, J.S., Jr., & Reed, G.H. (1972). Electromagnetic properties of hemoproteins. V. Optical and electron paramagnetic resonance characteristics of nitric oxide derivatives of metalloporphyrin-apohemoprotein complexes. *J. Biol. Chem.* **247**, 2447-2455.
30. David, P.R. (1991). A method for equilibrating protein crystals with heavy-atom reagents. *J. Appl. Crystallogr.* **24**, 1073-1074.
31. Howard, A.J., Gilliland, G.L., Finzel, B.F., Poulos, T.L., Olendorf, D.H. & Salemme, F.R. (1987). The use of an imaging proportional counter in macromolecular crystallography. *J. Appl. Crystallogr.* **20**, 383-387.
32. Otwinowski, Z. & Minor, W. (1996). Processing of X-ray diffraction data collected in oscillation mode. In *Methods in Enzymology Vol. 276 Macromolecular Crystallography, Part A.* (Carter, C.W., Jr. & Sweet, R.M., eds), pp. 307-326, Academic Press, San Diego, CA, USA.
33. Brünger, A.T. (1992). *X-PLOR Manual, Version 3.1: A System for X-ray Crystallography and NMR.* Yale University Press, New Haven, CT.
34. Evans, S.V. (1993). SETOR: hardware-lighted three dimensional solid model representation of macromolecules. *J. Mol. Graphics* **11**, 134-138.
35. Kraulis, P.J. (1991). MOLSCRIPT: a program to produce both detailed and schematic plots of protein structure. *J. Appl. Crystallogr.* **24**, 946-950.

Because *Chemistry & Biology* operates a 'Continuous Publication System' for Research Papers, this paper has been published via the internet before being printed. The paper can be accessed from http://biomednet.com/cbiology/cmb – for further information, see the explanation on the contents pages.